sensors

MDPI

Article

Using the EMFIT Sensor in Geophysical Monitoring

Victorin-Emilian Toader *, Constantin Ionescu, Iren-Adelina Moldovan and Alexandru Marmureanu

National Institute for Earth Physics, Călugăreni 12, 077125 Măgurele, Romania; viorel@infp.ro (C.I.); iren@infp.ro (I.-A.M.); marmura@infp.ro (A.M.)
* Correspondence: victorin@infp.ro

Abstract

EMFIT, also referred to as EMFi, is a ferroelectret film related to polyvinylidene fluoride (PVDF) sensors. It is an electroactive polymer (EAP) based on a polyolefin structure and consists of three layers of polyester film. Its application in geophysical monitoring has not been reported in the literature. At present, EMFIT is mainly employed in ballistocardiography and medical sleep monitoring, as developed by the manufacturer Emfit Ltd. (Vaajakoski, Finland). Within the multidisciplinary monitoring network of the National Institute for Earth Physics (NIEP), EMFIT is used as a pressure sensor in combination with infrasound transducers and microphones deployed in seismic areas. The primary aim of this study is to evaluate its suitability for detecting seismic noise that precedes earthquakes, generated by rock fracturing associated with crustal deformation. Although similar studies have been reported, they have not involved the use of EMFIT sensors. The novelty of this approach lies in the large surface area and mechanical flexibility of the material. Beyond seismic forecasting, the research also examines whether this type of sensor can contribute to seismic monitoring as a complement to conventional instruments such as accelerometers, seismometers, and microbarometers. Data analysis relies primarily on spectral time-series methods and incorporates measurements from other acoustic sensors (microphones and microbarometers) as well as a weather station. The working hypothesis is the potential correlation between the recorded data and the presence of enhanced noise prior to the detection of seismic waves by standard seismic sensors. The target area for this investigation is Vrancea, specifically the Vrâncioaia seismic station, where multidisciplinary monitoring includes infrasound, radon, thoron, soil temperature, and atmospheric electrical discharges. Preliminary tests suggest that the EMFIT sensor may function as a highly sensitive device, effectively serving as an "ear" for detecting ground noise.

Keywords: geophysical monitoring; acoustic emission monitoring; ferroelectret; PVDF

check for updates

Academic Editors: Raffaele Martorana and Alessandra Carollo

Received: 30 September 2025
Revised: 30 October 2025
Accepted: 3 November 2025
Published: 4 November 2025

Citation: Toader, V.-E.; Ionescu, C.; Moldovan, I.-A.; Marmureanu, A. Using the EMFIT Sensor in Geophysical Monitoring. *Sensors* **2025**, *25*, 6746. https://doi.org/10.3390/s25216746

Copyright: © 2025 by the authors. Licensee MDPI, Basel, Switzerland. This article is an open access article distributed under the terms and conditions of the Creative Commons Attribution (CC BY) license (https://creativecommons.org/licenses/by/4.0/).

1. Introduction

This study investigates the performance and potential of sensors produced by Emfit Ltd. (Vaajakoski, Finland) for applications in geophysical monitoring, with particular emphasis on seismic forecasting. Experimental tests examined the frequency response of the sensors, their sensitivity to environmental parameters (temperature, humidity, and atmospheric pressure), transfer function, and their comparative performance against established instruments, including infrasound sensors, seismometers, accelerometers, geophones, and pressure microphones. The overarching objective is to strengthen the network of seismic precursors deployed at the Vrâncioaia seismic station in the Vrancea region.

To date, no published studies have reported on the use of this type of sensor for such applications. The National Institute for Earth Physics (NIEP) maintains a multi-

disciplinary database containing measurements of the magnetic field, telluric currents, borehole and soil temperature, infrasound, CO_2, radon, ULF–VLF radio waves, and ground inclination, among others, collected through research projects exploring the feasibility of detecting earthquakes with magnitude Mw > 4 prior to their occurrence. Archived recordings acquired with EMFIT sensors, although unpublished, were also identified in the database. Re-examination of these data provided the impetus to resume this line of research, particularly in light of recent advances in digitalization and data processing.

Electromechanical film (EMFi) was invented in Finland in 1987 and represents the first cellular polymer electret film developed for commercial applications [1]. At present, EMFi or version EMFIT sensors are widely used in medical, surveillance, and healthcare fields, where they detect movement, activity, or physiological parameters such as blood pressure, pulse, respiration, vocal cord vibrations, and cardiac activity, as well as in smart bed systems for health and sleep monitoring [2–5].

The piezoelectric structure of EMFIT enables its dual use as a receiver and transmitter. It has been employed as a guitar microphone, as an actuator in audio systems, and in active noise cancellation (ANC) applications [2,6,7]. EMFIT has also been used as an ultrasonic transducer in radar systems [2,8], as a sonar head for autonomous robotic platforms [9,10], and in sports for measuring take-off force in ski jumping [11]. Another application involves smart seating, where sensors integrated into car seats enable contactless monitoring of vital signs, including capacitive electrocardiogram (cECG), ballistocardiography (BCG), and mechanical motion analysis [12].

The operating principle of EMFIT is based on thickness variations induced by external force or pressure, which generate electric charge and, consequently, a voltage across the electrodes [6,13]. Applications of acoustic and vibration-based electromechanical transducers have been reported across audio, ultrasonic, and infrasonic frequency ranges [14]. Furthermore, EMFIT has been integrated into active sound control (ACS) systems involving microphones and loudspeakers [7,15]. Since 1999, the VTT Technical Research Centre of Finland has developed and implemented EMFIT-based acoustic sensors and actuators in ACS and ANC applications, demonstrating effective noise reduction in buildings and transportation systems [16,17].

EMFIT sensors have also been applied in the automatic detection of lameness in cattle by analyzing pressure forces to differentiate between healthy and affected animals [18]. EMFi acoustic transducers developed by VTT have been investigated for airborne and underwater sound transmission, with superior results in air. It should be emphasized, however, that EMFi and EMFIT are not piezoelectric in the classical sense [19].

EMFIT belongs to the broader class of ferroelectrets, a term introduced by Bauer et al. [20] to describe materials combining the properties of ferroelectrics and space-charge electrets. This distinction is emphasized by Kärki and Lekkala [1] in their review of piezoelectric materials based on polyvinylidene fluoride (PVDF). They differentiate PVDF from cellular polymers such as EMFi, which mimic piezoelectricity through their electromechanical properties. The same authors conducted a comparative study of PVDF and EMFi sensor materials, highlighting their structural differences and distinct piezoelectric effects [21]. A concise review of ferroelectret materials is presented in [18], though EMFIT itself is not specifically mentioned. These materials have been utilized in air-coupled ultrasound transducers (ACUS) [22] and airborne ultrasonic arrays [23]. In robotics, ferroelectrets are particularly valued for tactile texture detection due to their thinness and mechanical flexibility [24]. The differences in sound quality between electret film (EMFIT) and piezoelectric guitar pickups are described by Miikka Tikander and Henri Penttinen in [25].

The similarity of EMFIT to piezoelectric sensors suggests its potential as a replacement for traditional geophones, with applications in detecting underground mining activity [26].

Related studies have examined the analysis of surface seismic waves (Rayleigh and Love) and the detection of anthropogenic emissions in the ELF band using piezoelectric films. Our research focuses on seismic noise generated by rock fracturing due to tectonic stress. EMFIT sensors could also be applied to landslide monitoring or the study of mud volcanoes in the Buzău region, in combination with CO_2 and radon measurements, which are already being performed. Recent work by Ming Li et al. [27] highlights advances in flexible PVDF-based piezoelectric sensors for applications in health, motion tracking, sports monitoring, human–machine interaction (HMI), smart homes, and vibration, though seismic applications are not addressed. PVDF films have also been employed for surface crack measurements using Rayleigh wave analysis in the frequency domain [28]. The importance of Rayleigh waves is further emphasized by Qingling Du et al. [29], who investigated their time–frequency characteristics in simulated and real seismic noise signals—an area directly relevant to our study. The potential to record Rayleigh waves with EMFIT sensors opens perspectives for tomography based on ambient noise and estimated Green's functions (EGF) [30,31]. Ambient seismic noise, together with surface waves, plays a critical role in probing Earth's interior, [32–35] even in urban environments [36]. The applicability of EMFIT sensors in this context, however, requires further validation. During initial tests, several teleseisms generated by Mw > 6 earthquakes at epicentral distances greater than 7000 km were recorded; however, this evidence remains insufficient.

Cazzulani et al. [37] investigated the feasibility of replacing acoustic emission (AE) sensors with piezoelectric PZT patches as a cost-effective alternative for monitoring crack propagation in concrete. Such research broadens the range of potential applications for EMFIT sensors in acoustic emission studies.

The NIEP monitoring network is multidisciplinary and includes, in addition to seismic and geophysical monitoring, the monitoring of building structures (such as road crossings, residential buildings, and dams). Structural Health Monitoring (SHM) is another area where EMFIT sensors can be used alongside existing equipment (accelerometers, gyro inclinometers, microphones, displacement sensors, geoelectric radars, GNSS, InSAR, Lidar) to determine the dynamic characteristics of buildings (natural frequency, damping) and to track the evolution of these parameters over time. The monitoring covers both natural (earthquakes, landslides) and anthropogenic phenomena, aiming to mitigate risks and protect the population in affected areas. The use of EMFIT sensors in this field is in its early stages and currently focuses on recording the noise produced by building structures during earthquakes. Seismic sensors only detect seismic waves and are limited to microphones with a sampling rate of 25 kHz to 50 kHz, which are useful for recording the 'scream' of concrete and beam reinforcement. In this study, we used Bode diagrams to determine the transfer function based on an explosion; any modification indicates a change in the building structure. The use of ferroelectret sensors with piezoelectric properties is mentioned in the specialized literature. Pengcheng Jiao et al. present in [38] the use of the piezoelectric effect in sensing methods to detect structural responses. In the article [39], a flexible piezo-ferroelectret sensor for structural health monitoring (SHM) is designed and fabricated based on the piezoelectric response of an electret film. It can be replaced with an EMFIT, which has similar properties, even though it is not truly piezoelectric. Tests on cement mortar indicate a linear relationship between the damage index and crack widths. In this case, the focus is on the occurrence of cracks and the noise they produce in rocks as a result of soil deformation. Pedro M. Ferreira et al. [40] analyzed the "design, fabrication, construction and implementation of embedded sensors (ES)". The aim is to monitor structures and structural components in real time and throughout their life cycle. In this application, they mention piezoelectric sensors (PS). The EMFIT could be embedded in concrete, respecting the linearity condition (5–60 N/cm^2). Ye Hai Li et al. [41] are investigating the use of

piezoelectric sensors in a monitoring network for monitoring the condition of multi-scale structures. EMFIT ferroelectrics can also be used in this context because they are flexible and can be customized in shape depending on the application. The main problem in the articles on SHM is that only the building is monitored, not the coupling with the ground. And the area where the foundation was built changes over time (settlement, the quality of the supporting surface is affected by water penetration, etc.).

A recent NIEP project aimed to locate explosions using microphones, which can be replaced with EMFIT sensors.

In summary, EMFIT sensors demonstrate versatility across a wide spectrum of applications, including seismic monitoring, although they are rarely mentioned in the existing literature. Our experimental tests, which included comparisons with acceleration, velocity, and infrasound sensors, provide insight into their response characteristics. The results suggest that EMFIT sensors hold promise for seismic forecasting and environmental noise analysis, complementing traditional instrumentation.

2. EMFIT Transducer and Experimental Tests

The EMFIT sensor is manufactured by Emfit Ltd. (Vaajakoski, Finland) in three configurations: L, R, and S. For research purposes, the company also provides EMFIT ferroelectret film, sometimes combined with ferroelectric films such as PVDF. In certain cases, sensor elements produced by Emfit Ltd. are incorporated into custom devices [42].

The EMFIT S-series sensor is a fully shielded device consisting of two layers of polyester film with screen-printed silver-paste electrodes. It is produced in both rectangular (10 × 20 mm) and circular (22 mm diameter) geometries (Emfit Ltd., S-series product page, https://www.sensors.emfit.com/copy-of-r-series-sensor accessed on 27 September 2025). The R-series sensors are fully shielded, low-mass, ribbon-type devices made from EMFIT ferroelectret film with three electrode layers on polyester films. Their standard dimensions are 19 mm in width, up to 6 m in length, and 0.4 mm in thickness (Emfit Ltd., R-series product page, https://www.sensors.emfit.com/copy-of-l-series accessed on 27 September 2025). The L-series sensors are fully shielded, thin, and large-area devices constructed from EMFIT ferroelectret film with three layers of polyester film and etched aluminum electrodes. Standard widths are 290 mm and 580 mm (Emfit Ltd., L-series product page, https://www.sensors.emfit.com/copy-of-publications-1 accessed on 27 September 2025).

EMFIT is an electroactive polymer (EAP) based on a polyolefin material manufactured through a continuous biaxial orientation process and expanded in thickness using a high-pressure gas diffusion–expansion (GDE) process (Emfit Ltd., printable EMFIT product page, https://www.sensors.emfit.com/copy-of-s-series-sensor accessed on 27 September 2025), [43]. This ferroelectret film represents the base element from which all sensor versions are constructed.

The present study employed the L-series sensor, as illustrated in Figure 1.

Changes in the thickness of the EMFIT sensor generate a voltage across the electrodes, as the device responds specifically to thickness variations rather than bulk deformation. Functionally, it can be regarded as an active capacitor exhibiting piezoelectric-like behavior [1].

The fabrication process of this type of sensor has been described in detail by the VTT Technical Research Centre of Finland [7,13,16,17,44]. A schematic representation of the fabrication steps of a ferroelectret tactile sensor is provided in [14,45–50]. Hamdi et al. [14] offer a comprehensive explanation of the origin and manufacturing procedures of piezoelectric cellular polymer films, including the development of the cellular structure, foaming stages, saturation, nucleation, expansion, and stabilization.

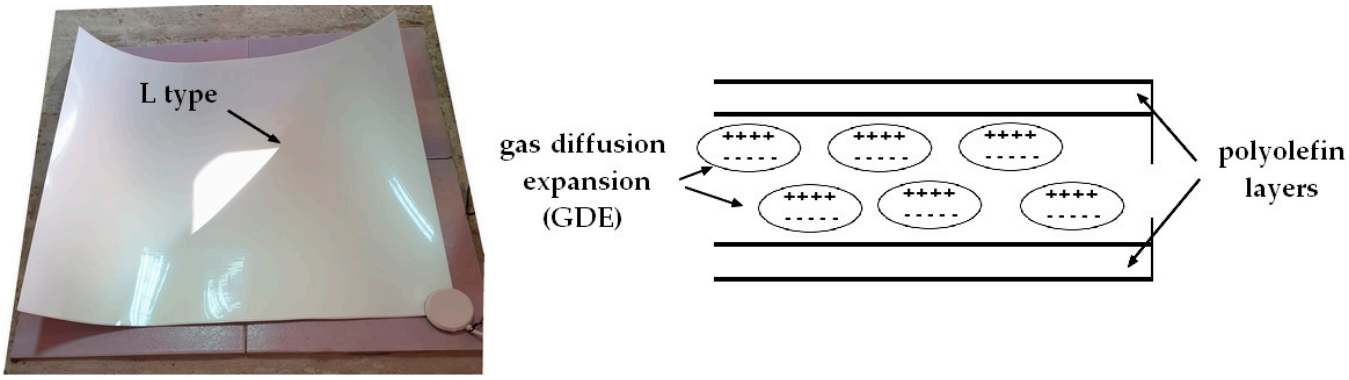


Figure 1. Emfit ferroelectret sensor, 3 layers of polyester film, L-series, simplified one air gap model (description https://www.sensors.emfit.com/copy-of-s-series-sensor accessed on 27 September 2025), microscopic image in [7].

Further contributions are noted in the broader literature. Bain and Chand, in the Transducers section, describe the EMFi film and ferroelectret sensors in general. More recently, Shi and Wagih [46] reported the first implementation of a wearable textile-based tactile sensor using polypropylene (PP) ferroelectret material for gesture recognition. In this work, PP film sheets produced by EMFIT Ltd. were integrated into gloves to enable contactless gesture detection.

2.1. Transducer Characteristics

The general characteristics of EMFIT sensors are presented in Table 1 the L-series used in tests.

Table 1. L-series sensor technical specifications (https://www.sensors.emfit.com/copy-of-publications-1, accessed on 27 September 2025).

Property	Symbol	Value	Unit	Tolerance	Conditions
Storage temperature	Ts	from −40 to +50	°C		
Operating temperature	Tr	from −20 to +70	°C		
Thickness	D	0.4	mm	±5%	
Sensitivity [1]	Sq	25	pC/N	±20%	normal force
Relative permittivity	er	1.1		±10%	@ 10 kHz
Capacitance	C	22	pF/cm^2	±5%	@ 1–150 kHz, EQV
Tensile strength at break, TD		535	N	±10%	ISO-527-1
Elongation at break, TD		20	%	±20%	
Young modulus, TD		1	MPa	±50%	
Operating force range	P	<300	N/cm^2		
Standard width	W	290/580	mm	±1%	
Sample length [2]	L	300	mm	±1%	

[1] Loss of sensitivity is <20% after the following temperature cycles as follows: 11 h at −20 °C, 1 h at +20 °C, 11 h at +70 °C, 1 h at +20 °C, 28 cycles; and 1 h at −20 °C, 1 h at +70 °C, 10 cycles. [2] Manufactured in rolls, width 580 mm, divided into rectangular areas with a size of 290 × 300 mm, which are electrically connected. Can be cut to shorter sensors.

Changes in the thickness determine the output voltage ΔV of an EMFIT sensor:

$$\Delta V = (1/C) \times S_q \times \Delta F \quad (1)$$

where C is the capacitance, Sq the sensitivity of the sensor and ΔF the applied force [51].

$$S_q = \Delta\sigma/\Delta p \quad (2)$$

where Δσ is the change in the charge density on the electrodes and Δp = ΔF/Ad is the amplitude of the dynamic pressure within the area Ad where the force is acting [2].

Equations (1) and (2) are only valid when the sensor is operating within its linear region. Table 1 specifies the operating force range, P < 300 N/cm^2, and the operating temperature from −20 to +70 °C. The document [52] shows that EMFIT sensors are linear at least between 5 and 60 N/cm^2 (standard deviation was <5%). It is also stated that the linearity depends on the number of EMFIT layers and the adhesives used to assemble the sensors.

Generally, the ferroelectret sensors' size, dimension, surface, and direction of excitation [53], are important in AE applications, which is an advantage for EMFIT. Rayleigh waves (RW) receiving sensitivities depend on sensor size [54].

The experiments presented in this study were performed using an EMFIT L-series device (60 × 60 cm) supplied by Emfit Ltd. (Vaajakoski, Finland). The system was delivered with an impedance adapter and a preamplifier, providing sensitivities of 53 pC/N, 19.08 pC/Pa, and 86.7 µV/Pa, together with an analog high-pass filter with a cutoff frequency of 0.007 Hz.

The Chaparral Model 64 S is the reference equipment. The verification of EMFIT sensors in the infrasound spectrum is being pursued. Its technical specifications are in Table 2 (Operation manual for the Model 64 S Infrasound Sensor for use in the wide infrasound band, Chaparral Physics, Manual Revision 1, 28 April 2022).

Table 2. Chaparral Model 64 S Specifications.

Nominal Sensitivity: Standard	**0.08 Volts/Pa @ 1 Hz, 250 Pa Full Scale Range**
Output: Output type	Differential
Maximum	20 volts peak-to-peak (signal+ to signal−), 10 volts max signal to ground. With no signal applied, the outputs idle at +5.5 V
Frequency Response Self-noise	Flat to within 3 dB from 0.01 Hz to 245 Hz. Less than 1.3 × 10^{-7} Pa^2/Hz @ 1 Hz (−69 dB, relative to 1 Pa), Less than 1.7 mPa RMS 0.1 to 200 Hz, less than 0.5 mPa RMS 0.5 to 2 Hz
Dynamic range	110 dB @ 0.5 Hz to 2 Hz
Output Impedance	150 Ω non-reactive, (recommend load > 10 kΩ) (Recommended less than 1.0 µF capacitive loading).
Short circuit protected	Momentary shorts from signal+ to signal−, and signal to ground
Power Requirements: DC Source	12 volts (11.25–20 volts) DC, reverse voltage protected. Battery-powered operation is recommended to optimize noise performance.
Current Drain	Less than 15 mA @ 12 V (Less than 168 mW)
Physical	The sensor will function in any position or attitude. Sealed to IP-67 with acoustic inlets sealed and mating electrical connector or cap installed. Preferred orientation for proper venting: manifold
Operating Temperature	down −40 °C to +65 °C

Table 2. *Cont.*

Nominal Sensitivity: Standard	**0.08 Volts/Pa @ 1 Hz, 250 Pa Full Scale Range**
Humidity	95% (non-condensing).
Dimensions	3.86″ diameter, 3.1″ tall (not including the Garden Hose Inlets) (9.8 cm diameter, 7.8 cm tall)
Weight	1.25 lbs (0.57 kg)
Std Acoustic inlets	3-port manifold, standard US Garden Hose Thread

The primary objective of these tests was to evaluate whether EMFIT sensors can be employed for earthquake forecasting in conjunction with other dedicated monitoring instruments. Preliminary evidence from the NIEP archive supports this hypothesis. Figure 2 presents a representative recording obtained with this type of sensor in Vrâncioaia station.

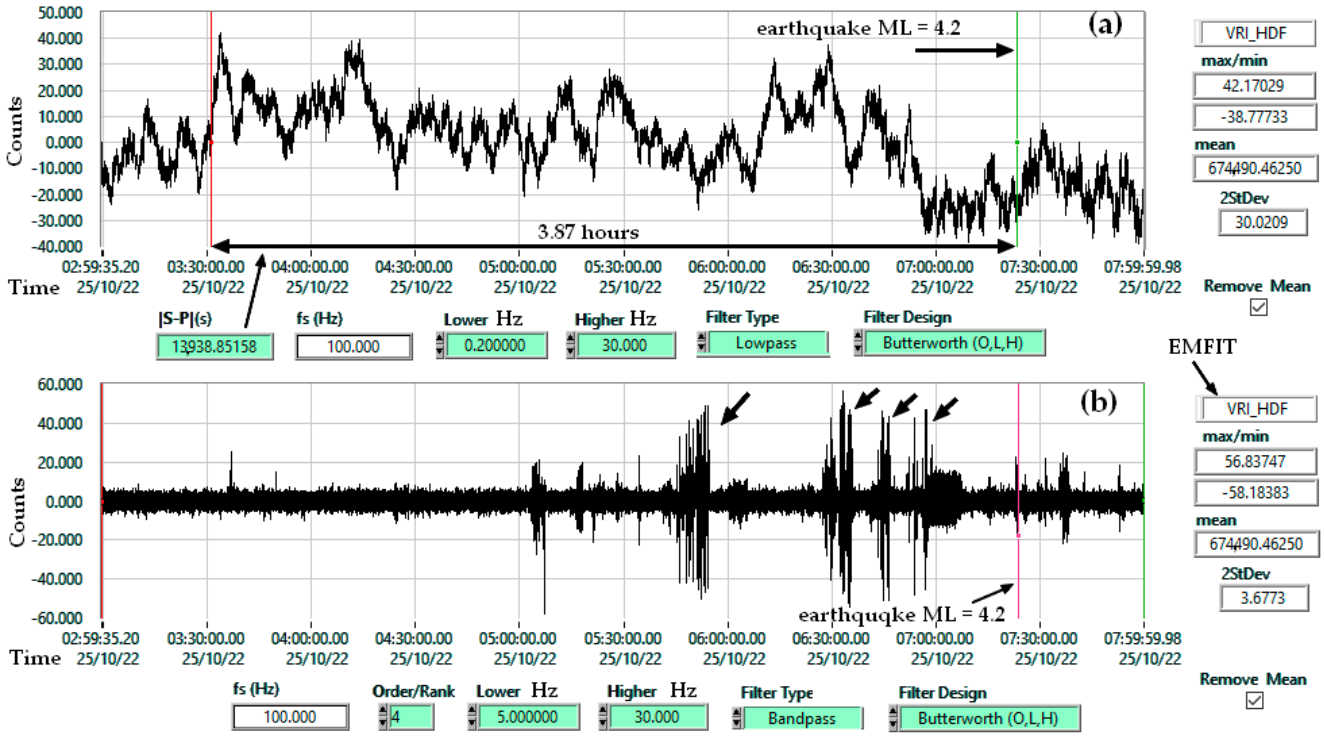


Figure 2. Emfit sensor (VRI_HDF) used in geophysical monitoring, earthquake ML 4.2, Latitude 45.8420, Longitude 26.6994, Depth 90.1 Km, 22 October 2025 07:23:26; (**a**) Lowpass Filter 0.2 Hz; (**b**) Bandpass Filter 5–30 Hz.

In case (a), the first change in the amplitude of the time series filtered with a low-pass filter occurs almost 4 h before the earthquake. At low frequencies, a change in pressure on the sensor is more noticeable. In case (b), the focus is on highlighting the seismic noise specific to rock breakage. This noise is observed when testing construction materials at the moment of breakage under controlled pressure.

2.2. Experimental Tests

Comparative tests were conducted using infrasound sensors (Chaparral and LPM 5481–Druck), mounted in both horizontal and vertical orientations. Since the NIEP network includes infrasound arrays, it was essential to assess whether EMFIT sensors could adequately cover this frequency range. For reference, the same test room also housed a

seismometer and an accelerometer. Figures 3 and 4 illustrate the experimental setup and instrumentation.

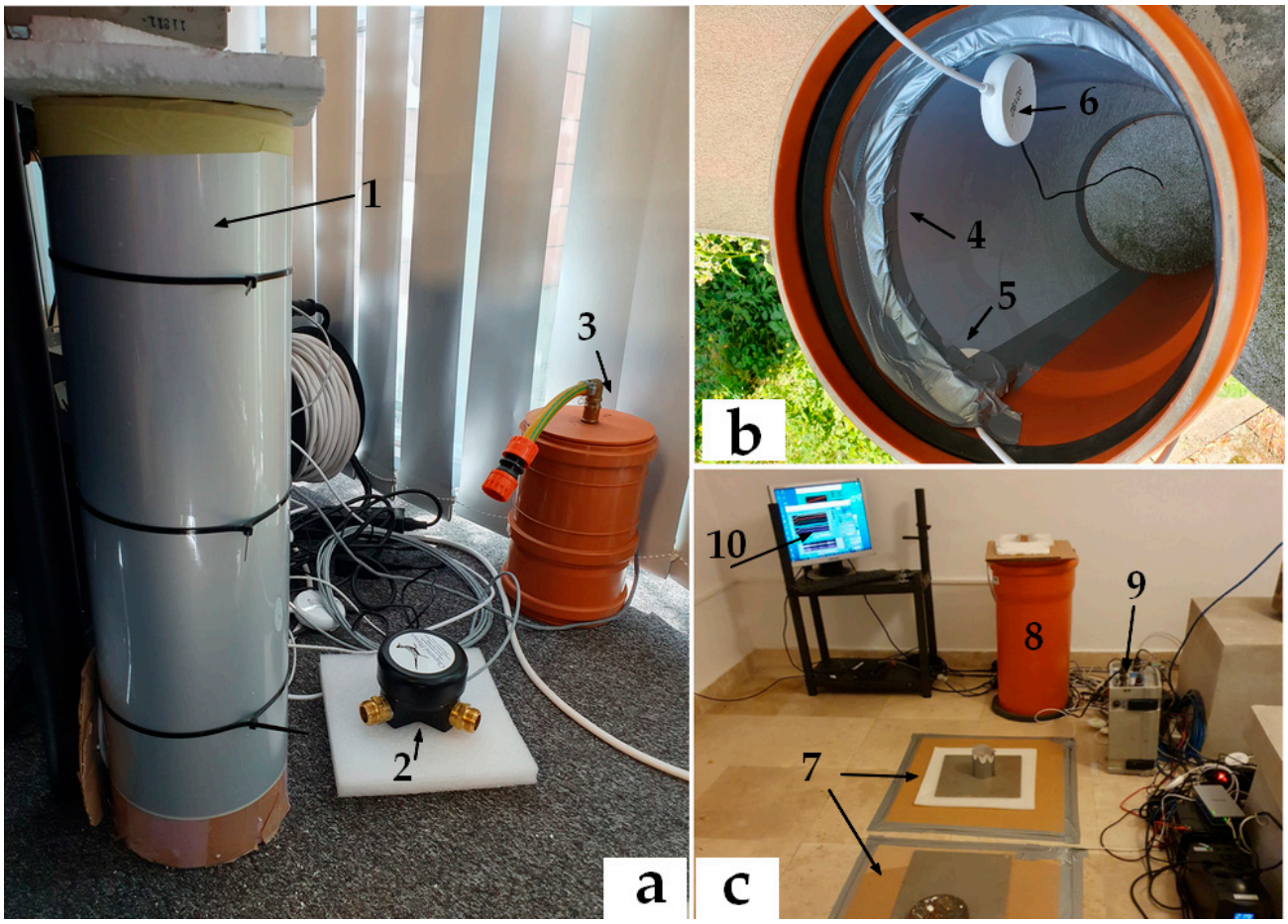


Figure 3. Test Emfit sensor: (**a**) (1) EMFIT sensor mounted externally on a vertical tube; (**a**) (2–3) infrasound equipment; (**b**) EMFIT sensor mounted internally; (**c**) horizontal installation.

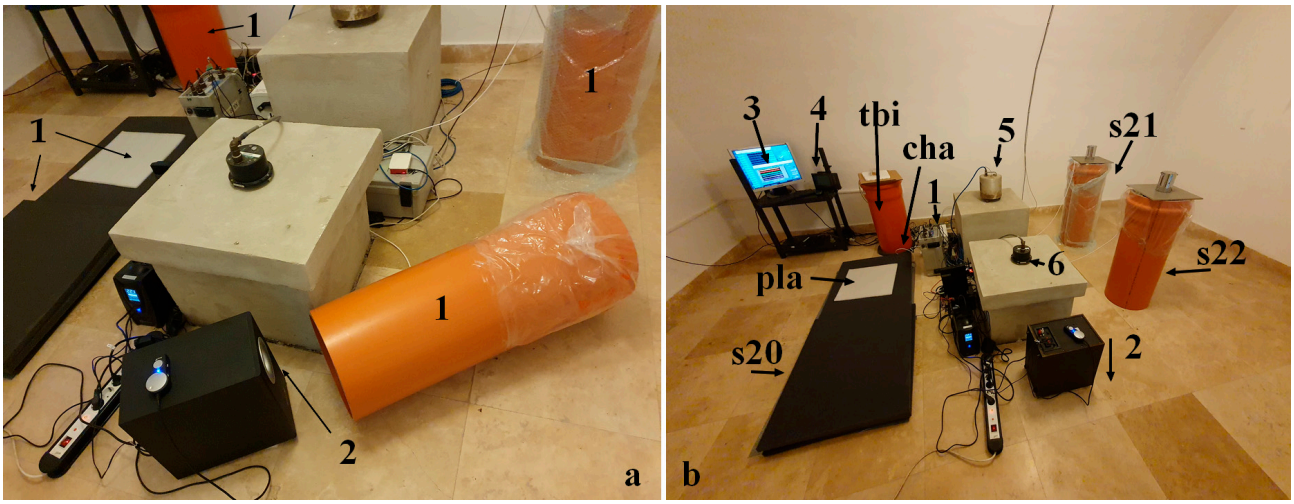


Figure 4. Experimental configuration; (**a**) EMFIT sensors mounted horizontally and vertically with an acoustic vibration generator; (**b**) test chamber configuration.

The infrasound measurement tubes were constructed from PVC (polyvinyl chloride) with lengths ranging from 0.71 m to 1 m and an inner diameter of 0.315 m. Because the EMFIT sensor responds specifically to changes in its thickness, only one side of the film

was exposed to ambient vibrations, while the opposite side was insulated. Mounting the sensor directly on a flat surface facilitates this isolation but requires more space. By contrast, the tube-based configuration is more compact, requiring only fixation with silicone. To minimize internal wave reflections, a sponge was inserted at the upper end of the tube, while the lower end was sealed, ensuring that the sensor recorded vibrations exclusively from below.

Numerous methods for sensor calibration are reported in the literature. Among these, the face-to-face transmitter–receiver method is described by Kanji Ono [55], along with reciprocity calibration methods, which are well established for acoustic transducers (hydrophones and ferroelectret devices). A related approach is the surface-to-surface method [56], which was employed in the present tests: a source transducer generated vibrations simultaneously recorded by a reference sensor and the EMFIT device under test. The reciprocity calibration method for acoustic emission transducers has been widely [55,57–61], although it is constrained by the Hill–Adams equation [55]. Rayleigh waves have also been used in acoustic emission calibration, as reported by Hatano [57] and others [54,58].

The experiments in this study focused on the frequency response of EMFIT sensors in the 5–45 Hz range. Similar comparative tests are described in the literature, including the characterization of EMFi microphones against reference B&K microphones [6], and multilayer EMFIT configurations (one, two, and three layers) [42]. Frequency response analysis using the surface-to-surface calibration method has also been presented by Prevorovsky and colleagues [56,62].

Figures 3 and 4 illustrate the sensor configurations tested. In Figure 3a, the EMFIT sensor (1) was mounted on the exterior of a vertical tube, with Chaparral (2) and LPM 5481–Druck (3) sensors serving as references. Figure 3b shows the EMFIT sensor inside a vertical tube (4), connected to the impedance adapter (5) and preamplifier (6). In this case, vibrations were captured within the tube - a configuration not previously reported in the literature. Typically, EMFIT sensors are used in horizontal orientation, as shown in Figure 3c, (7). The same figure also depicts an EMFIT sensor mounted inside a tube (8) with a Chaparral transducer at its base, a 24 bits Kinemetrics K2 digitizer (9), and data acquisition software (10). The vibration source was provided by a software signal generator and an audio amplifier.

In Figure 4a, EMFIT sensors (1) were positioned both horizontally and vertically, with the audio speaker acting as the vibration source (2). The final configuration is shown in Figure 4b, where EMFIT sensors are marked according to the schematic (tbi = inner tube, cha = Chaparral, etc.). The vibration source (2) was oriented toward the floor, while environmental parameters (temperature, humidity, and pressure) were monitored by a weather station (4). An accelerometer and a seismometer, mounted on concrete pillars, are shown at positions (5) and (6), respectively. The ceiling of the test chamber has a semi-cylindrical shape with flat ends.

Because EMFIT sensors generate an electrical charge in response to changes in thickness, proper mounting is critical. Only one side of the sensor must be exposed to the vibration source, while the opposite side must remain insulated.

The signal generator was implemented in software (Figure 5(1)), providing test frequencies from 5 Hz to 45 Hz in 1 Hz increments. The preamplifier supplied with the EMFIT sensors has an upper cutoff frequency of 50 Hz, which, according to the Nyquist theorem, implies a sampling frequency of 100 Hz.

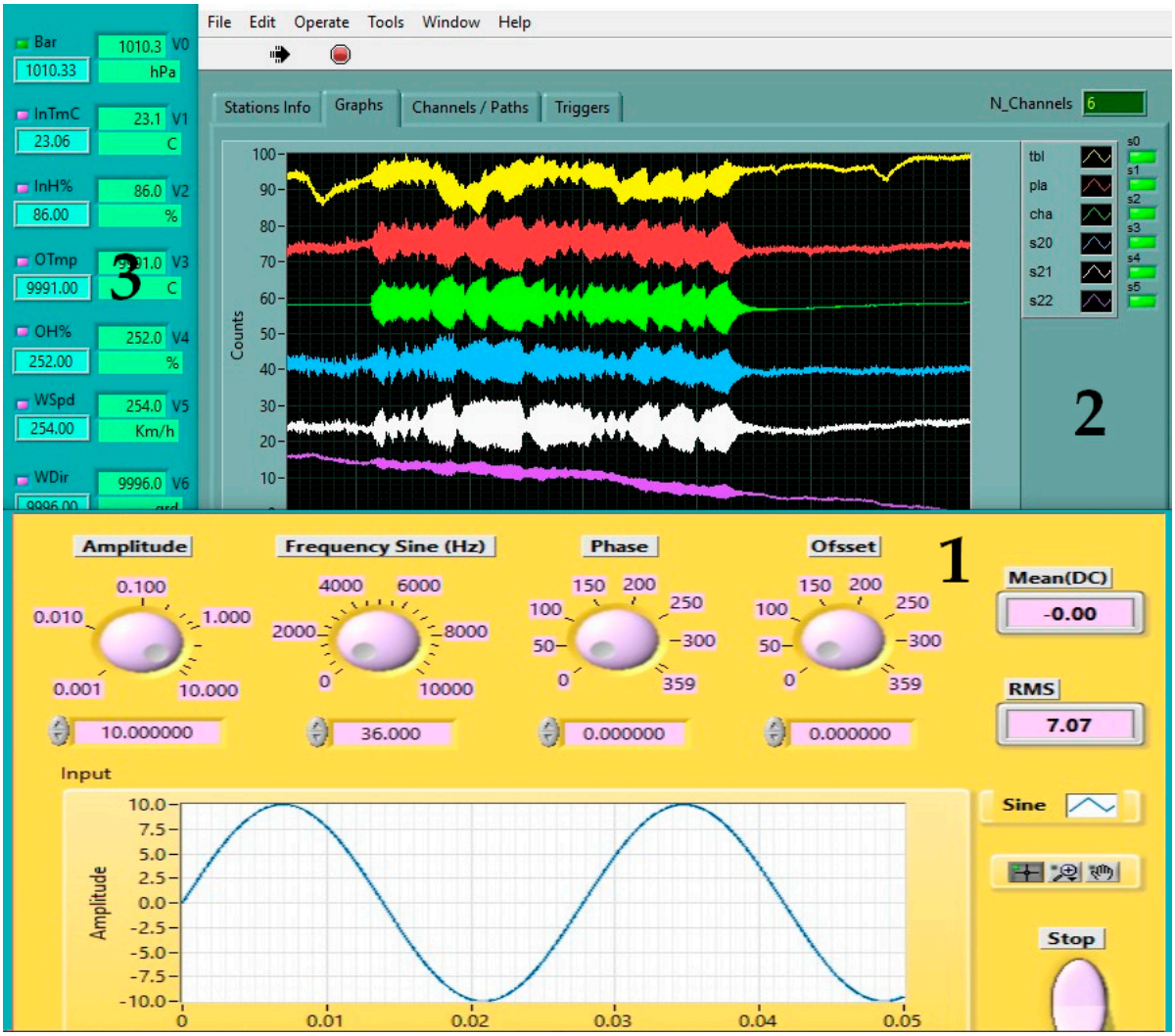


Figure 5. Experimental setup: (**1**) virtual signal generator; (**2**) data acquisition software; (**3**) meteorological monitoring station.

Data acquisition software (Figure 5(2)) recorded waveforms in SAC–BIN format. Environmental dependencies were monitored using a meteorological station (Figure 5(3)). A resonance peak at 36 Hz was observed under the test conditions.

3. Results

Tubes used for mounting EMFIT sensors exhibit resonant frequencies that may influence measurements. Depending on the design, the tubes may be open at both ends, open at only one end (Figure 4a), or completely closed (Figure 4b). The sensors can be mounted externally (Figure 3a) or internally (Figure 3b,c), provided that one side is insulated from external vibrations.

For a closed cylinder, the resonant frequency is given by the relationship ([63]):

$$f = \frac{n \times v}{4 \times (L + 0.3 \times d)} \quad (3)$$

where

f = resonant frequency, Hz;
n = harmonic 1, 3, 5 . . .;
v = speed of sound, 340 m/s;

L = tube length, m;
d = tube diameter, m;

0.4 X d represents the end correction of a closed tube or pipe.

For L = 0.71 m and d = 0.315 m (as in Figures 3 and 4), the first resonant frequency is 105.65 Hz, outside the test range. For the maximum tube length of 1 m, the first resonance is 77.66 Hz, still above the frequencies tested.

Figure 6 illustrates an example of a frequency response test for the 31–40 Hz range, although the experiments were performed from 5 to 45 Hz with 1 Hz increments. A clear maximum at 36 Hz is visible in both the Power Spectral Density (PSD) and the Short-Time Fourier Transform (STFT) spectrogram.

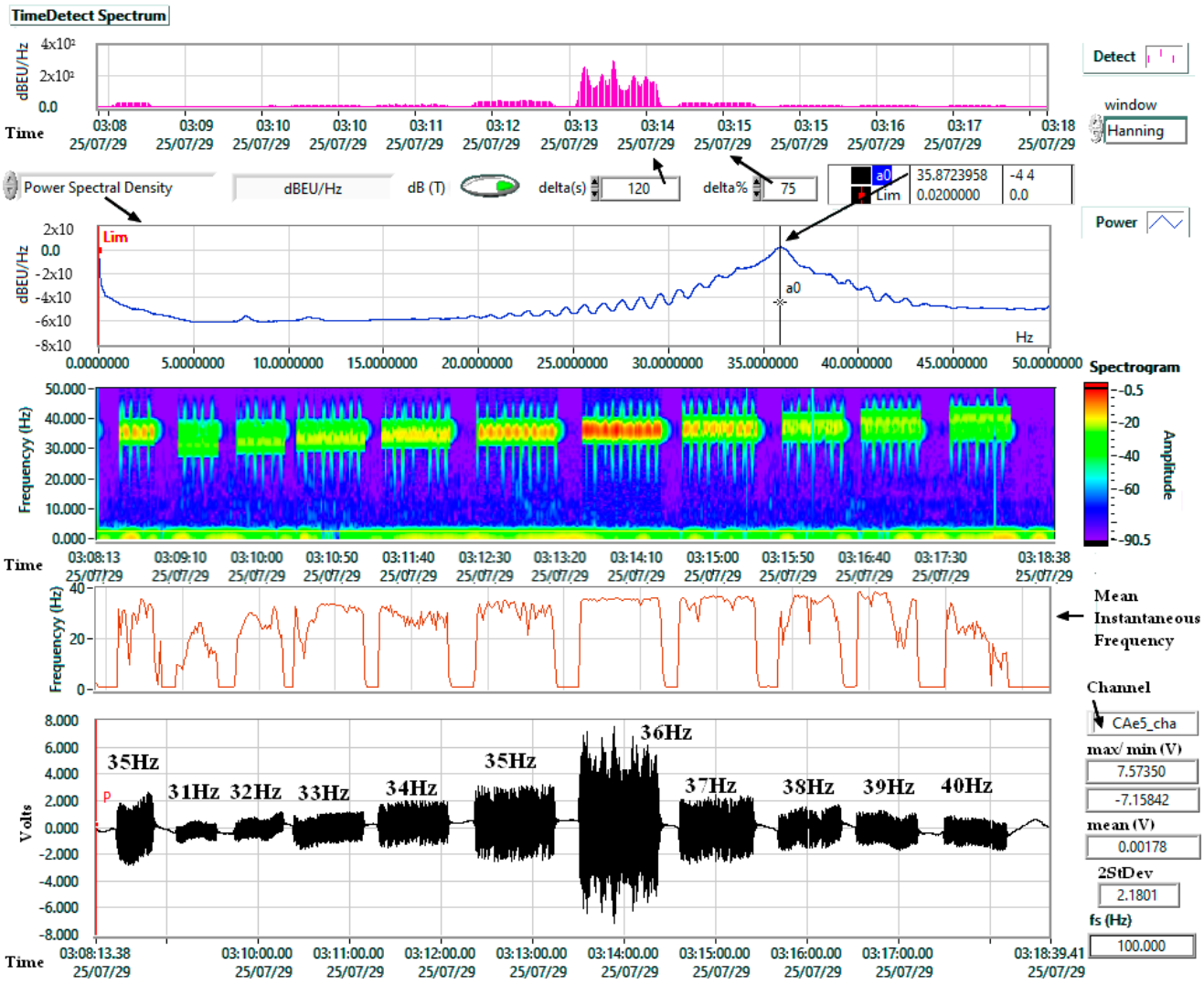


Figure 6. Test signals, frequency response of the Chaparral (cha) sensor, example for the range 31–40 Hz.

Each frequency was analyzed using a ±2 Hz Butterworth band-pass filter (Figure 7).

RMS values and double the standard deviation (2σ or 2StDev), a parameter widely adopted as a threshold indicator [64,65], were calculated for each sensor shown in Figure 4b. The results are summarized in Table 3.

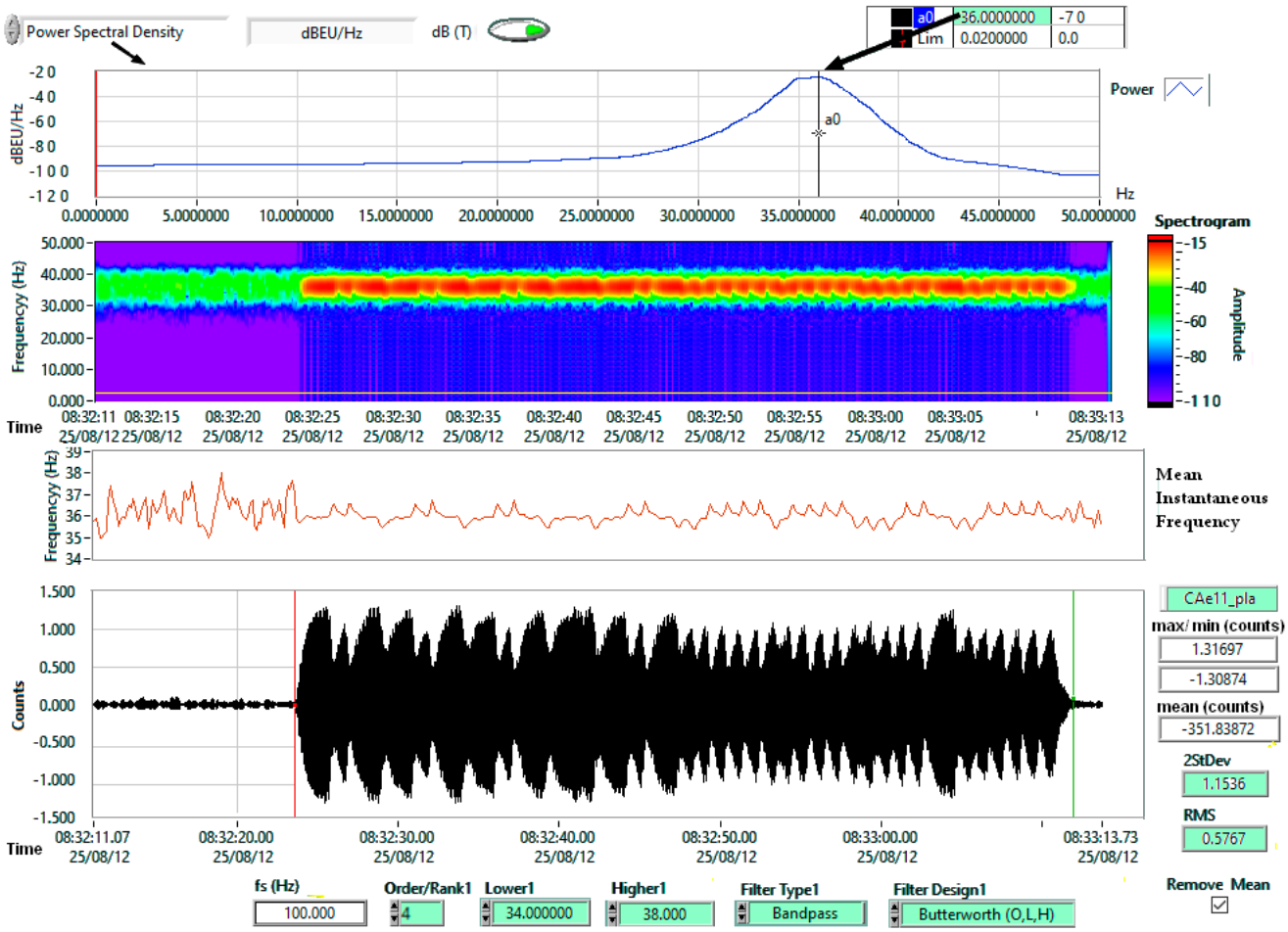


Figure 7. Test signal, frequency response of the Emfit sensor 'pla' (Figure 4b) for 36 Hz.

Table 3. Frequency response of EMFIT sensors, filter used bandpass Butterworth +/− 2Hz relative to testing frequency. The locations of the sensors are shown in Figure 4.

Sensor	cha		pla		s20		s21		s22		tbI	
f(Hz)	RMS	2StDev	RMS	2StDev	RMS	2StDev	RMS	2StDev	RMS	2StDev	RMS	2StDev
5	0.0144	0.0287	0.0285	0.057	0.057	0.0474	0.0254	0.0508	0.0253	0.0507	0.0246	0.0493
6	0.0248	0.0496	0.0339	0.0678	0.0321	0.0642	0.0309	0.0618	0.0313	0.0626	0.0349	0.0697
7	0.0775	0.1551	0.0787	0.1573	0.0738	0.1475	0.0745	0.1491	0.0732	0.1465	0.0808	0.1617
8	0.3879	0.7759	0.3769	0.7539	0.3434	0.6868	0.3563	0.7126	0.349	0.6981	0.3762	0.7525
9	0.1335	0.2671	0.1289	0.2578	0.1169	0.2337	0.1237	0.2475	0.12	0.2399	0.1294	0.2588
10	0.0855	0.171	0.0832	0.1664	0.0747	0.1494	0.0806	0.1613	0.0766	0.1531	0.0842	0.1684
11	0.0934	0.1868	0.0895	0.179	0.0794	0.1589	0.0868	0.1736	0.0808	0.1617	0.0912	0.1825
12	0.1626	0.3252	0.1536	0.3072	0.1335	0.2671	0.1476	0.2952	0.1345	0.2689	0.1565	0.3129
13	0.1294	0.2589	0.1212	0.2424	0.1036	0.2072	0.1192	0.2385	0.1035	0.207	0.1245	0.249
14	0.1281	0.2563	0.1193	0.2387	0.0987	0.1975	0.1192	0.2385	0.0996	0.1993	0.1238	0.2475
15	0.1224	0.2449	0.1157	0.2314	0.0954	0.1908	0.117	0.234	0.0957	0.1913	0.1181	0.2363
16	0.1164	0.2329	0.1107	0.2215	0.0893	0.1786	0.1132	0.2265	0.0923	0.1847	0.113	0.2259
17	0.1193	0.2386	0.1093	0.2186	0.0866	0.1732	0.1139	0.2278	0.0901	0.1802	0.1131	0.2263

Table 3. *Cont.*

Sensor	cha		pla		s20		s21		s22		tbI	
f(Hz)	RMS	2StDev	RMS	2StDev	RMS	2StDev	RMS	2StDev	RMS	2StDev	RMS	2StDev
18	0.1299	0.2598	0.1118	0.2237	0.088	0.1761	0.1177	0.2354	0.095	0.19	0.1222	0.2445
19	0.136	0.2721	0.1141	0.2283	0.0877	0.1755	0.1209	0.2418	0.0946	0.1892	0.1277	0.2554
20	0.1445	0.2889	0.1176	0.2352	0.0879	0.1759	0.1177	0.2355	0.0937	0.1873	0.1344	0.2688
21	0.1501	0.3003	0.1198	0.2396	0.0898	0.1795	0.1189	0.2378	0.0889	0.1779	0.141	0.282
22	0.1492	0.2984	0.1166	0.2333	0.0843	0.1686	0.1157	0.2314	0.0857	0.1713	0.1393	0.2786
23	0.1496	0.2993	0.116	0.232	0.0852	0.1704	0.1129	0.2259	0.0906	0.1812	0.1408	0.2817
24	0.1611	0.3222	0.1234	0.2467	0.0939	0.1878	0.1147	0.2295	0.0886	0.1772	0.1515	0.3029
25	0.1742	0.3484	0.1292	0.2584	0.0850	0.1701	0.1198	0.2397	0.0773	0.1546	0.1618	0.3236
26	0.1584	0.3168	0.1170	0.2340	0.0727	0.1454	0.1076	0.2153	0.0558	0.1116	0.1480	0.2960
27	0.1753	0.3506	0.1263	0.2526	0.0741	0.1481	0.1134	0.2268	0.0567	0.1134	0.1623	0.3246
28	0.1819	0.3638	0.1292	0.2585	0.0713	0.1426	0.1141	0.2282	0.0516	0.1033	0.1672	0.3344
29	0.1817	0.3634	0.1283	0.2567	0.0700	0.1399	0.1087	0.2175	0.0483	0.0966	0.1674	0.3347
30	0.1894	0.3788	0.1311	0.2622	0.0714	0.1428	0.1038	0.2077	0.0411	0.0822	0.1726	0.3453
31	0.2032	0.4063	0.1407	0.2814	0.0785	0.1570	0.0984	0.1968	0.0399	0.0798	0.1865	0.3731
32	0.2475	0.4950	0.1668	0.3337	0.0999	0.1998	0.0995	0.1990	0.0375	0.0751	0.2229	0.4459
33	0.2881	0.5762	0.1985	0.3970	0.1246	0.2492	0.0842	0.1685	0.0588	0.1177	0.2585	0.5171
34	0.3197	0.6395	0.2345	0.4691	0.1519	0.3037	0.0837	0.1674	0.1103	0.2206	0.2913	0.5827
35	0.4783	0.9567	0.3733	0.7466	0.2588	0.5177	0.2131	0.4263	0.2596	0.5193	0.4254	0.8508
36	0.6502	1.3005	0.5767	1.1536	0.4670	0.9340	0.6738	1.3477	0.5723	1.1446	0.5758	1.1517
37	0.2426	0.4853	0.2128	0.4257	0.2072	0.4144	0.4438	0.8876	0.2949	0.5899	0.2169	0.4339
38	0.1829	0.3659	0.0926	0.1852	0.1028	0.2056	0.3145	0.6291	0.1622	0.3243	0.1615	0.3231
39	0.1870	0.3740	0.0734	0.1468	0.0718	0.1437	0.2488	0.4977	0.1014	0.2028	0.1642	0.3284
40	0.1688	0.3376	0.0655	0.1310	0.0518	0.1037	0.1934	0.3868	0.0735	0.1470	0.1470	0.2939
41	0.1447	0.2895	0.0565	0.1129	0.0411	0.0822	0.1444	0.2887	0.0517	0.1033	0.1255	0.2509
42	0.1064	0.2128	0.0422	0.0843	0.0277	0.0553	0.0997	0.1995	0.0357	0.0714	0.0920	0.1839
43	0.0710	0.1421	0.0290	0.0581	0.0195	0.0391	0.0639	0.1277	0.0196	0.0391	0.0611	0.1223
44	0.0359	0.0719	0.0151	0.0301	0.0106	0.0212	0.0302	0.0603	0.0091	0.0181	0.0308	0.0615
45	0.0180	0.0359	0.0081	0.0161	0.0058	0.0117	0.0147	0.0294	0.0053	0.0107	0.0158	0.0317

Standard deviation (σ) is critical for estimating measurement standard uncertainty [66–68]. Within ±2σ, there is approximately a 95.4% probability that the true value lies within this range (https://itu.physics.uiowa.edu/courses/reporting-uncertainties accessed on 27 September 2025). Twice the standard deviation (±2σ) is applied in many cases, like a trigger limit [69–72].

Figures 8 and 9 provide a visual representation of the results. Figure 8 shows the frequency response of horizontally mounted EMFIT sensors (pla and s20, Figure 4b) in comparison with the Chaparral reference sensor (cha, Figures 3c and 4b).

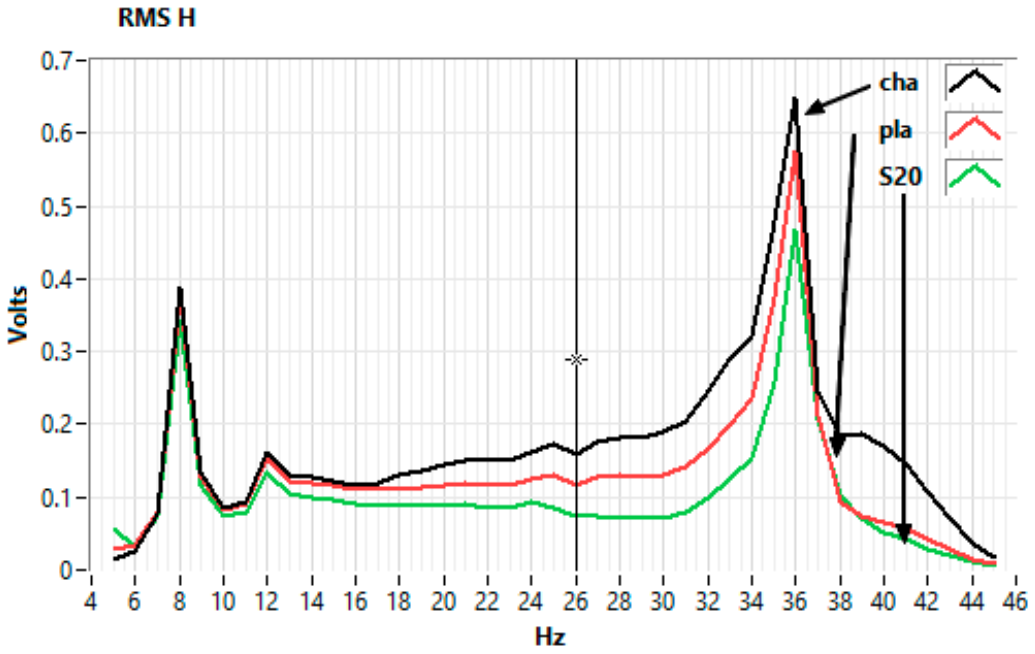


Figure 8. Frequency response of the horizontally mounted Emfit sensors (pla, s20) and the Chaparral reference (cha).

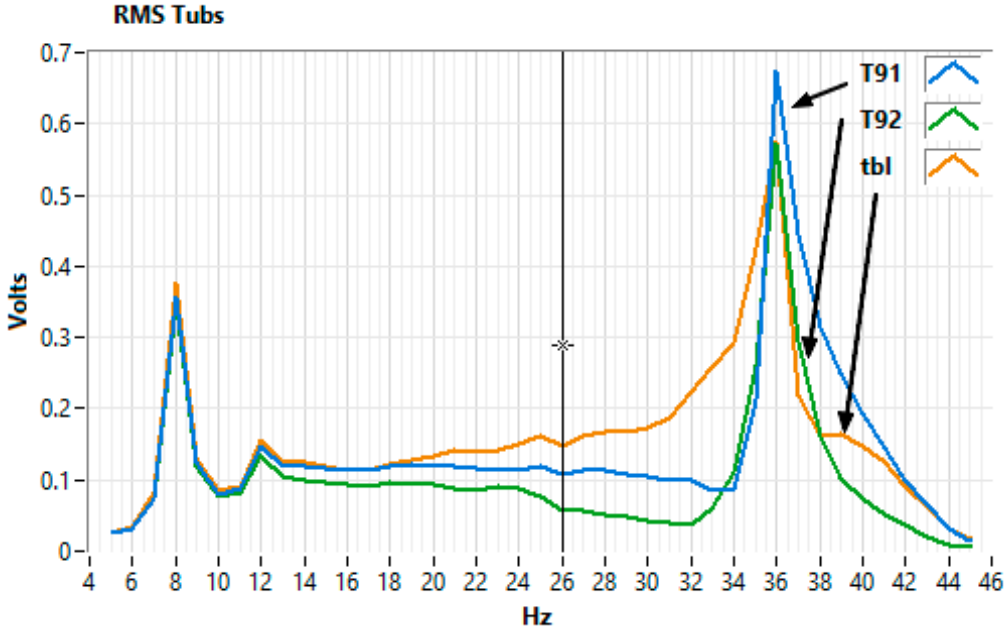


Figure 9. Frequency response of Emfit sensors mounted vertically in tubes (tbi, s21, s22).

Figure 9 presents the response of EMFIT sensors mounted vertically inside tubes (s21 and s22, Figure 4b). In both cases, the response curves closely resemble those of the Chaparral reference.

Environmental dependencies were monitored with a meteorological station (Figure 4b(4)). Figure 10 shows daily variations in EMFIT and Chaparral sensor output.

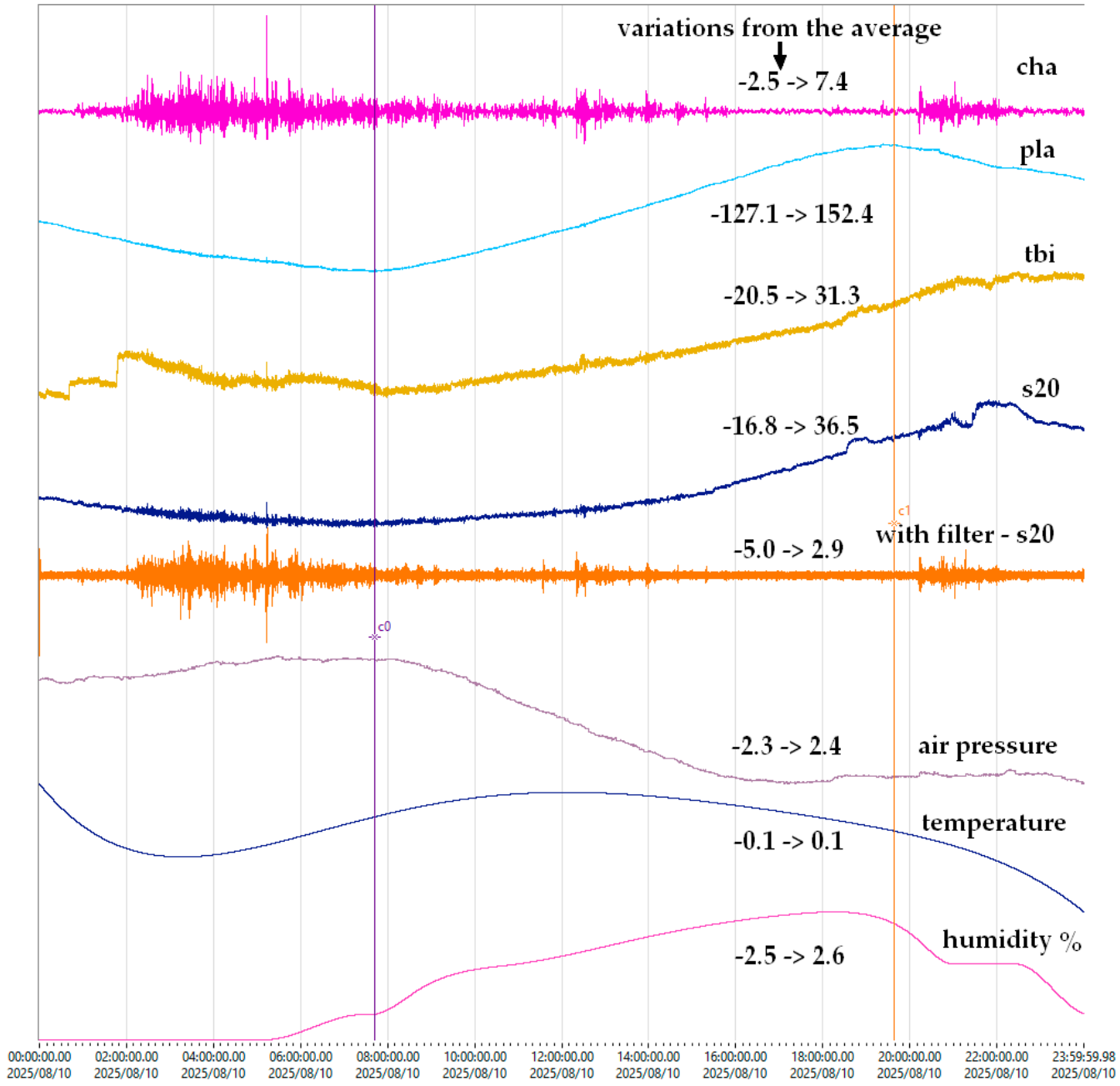


Figure 10. Dependence of Emfit sensors on environmental conditions.

The filtered signal "s20" demonstrates a clear correlation with the Chaparral sensor, confirming environmental influence. Further, Figure 11 demonstrates the recording of Rayleigh waves from a distant earthquake in Kamchatka (epicentral distance > 7000 km), comparing seismometer, infrasound, and EMFIT signals.

The unfiltered EMFIT signal in Figure 11 shows that it has a larger bandwidth than the Chaparral infrasound. After removing the local noise by filtering, a waveform similar to a maximum on the S of the seismic wave results, but the amplitudes are still small.

Figure 12 presents a 6.2 Mw earthquake in the Sea of Marmara (23 April 2025, 09:49 UTC), recorded by seismometers, geophones, infrasound sensors, and EMFIT sensors mounted both in tubes and flat on the ground (Figure 3a).

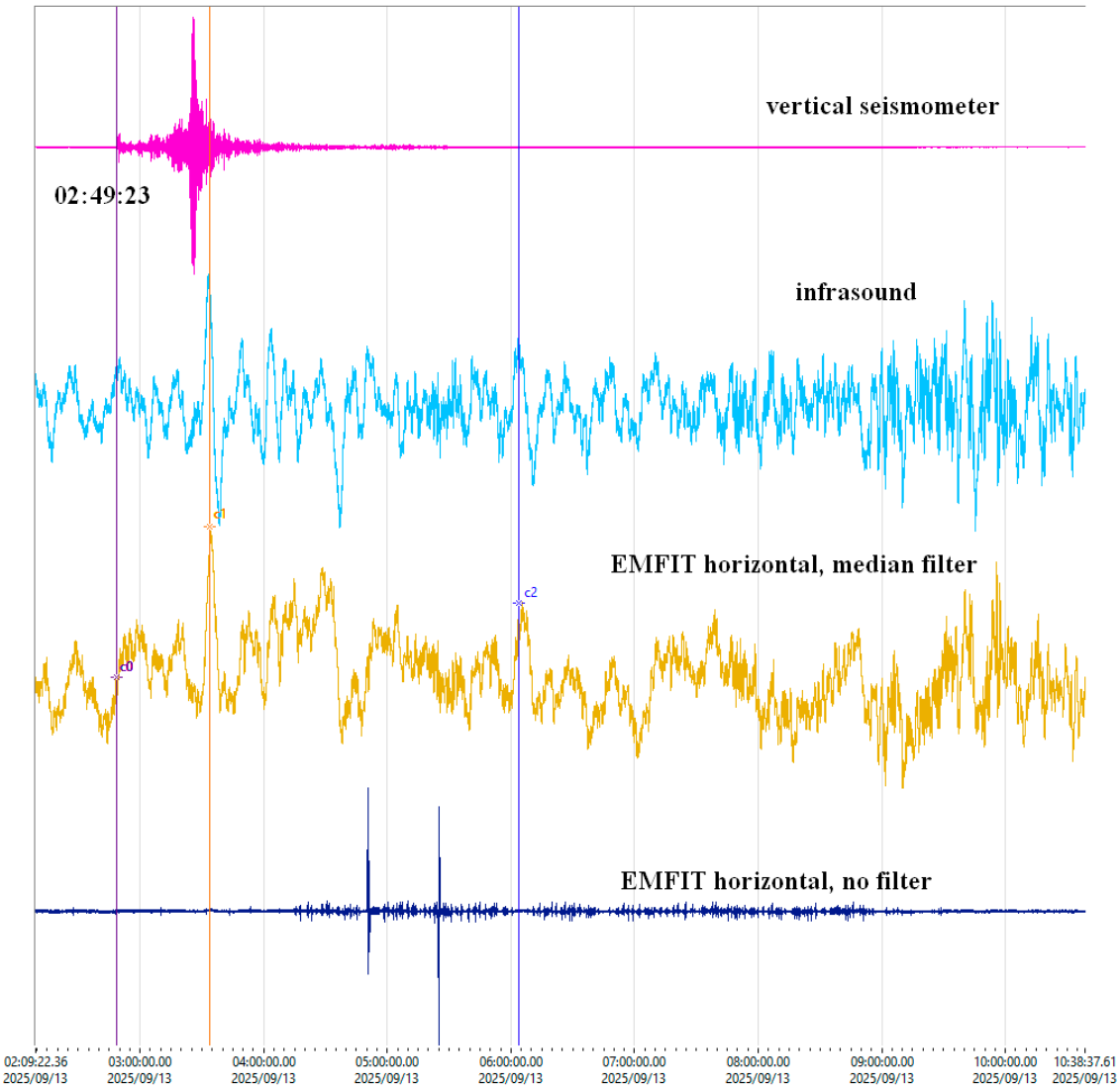


Figure 11. Recording of Rayleigh waves produced by an earthquake located in Kamchatka by an infrasound sensor and an Emfit.

The example in Figure 12 refers to an earthquake with the epicenter located approximately 480 km from the location where the recording was made. It demonstrates that the best results can be obtained with EMFIT sensors if the vibrations reach their surface and produce a change in their thickness. In the case of Figure 12, this was achieved with an object that oscillated on the surface of the film and a tube that vibrated. The geophone response has a small amplitude, even though it was placed on the EMFIT sensor flat.

JIRI KEPRT and PETR BENES compare the main methods for calibrating acoustic emission (AE) sensors in this article [73]. A calibration method is standardized by ASTM E 178 and ASTM E 976 [74] and requires a reference sensor with known characteristics. Calibration involves comparing the results from the reference transducer and the transducer under test. The transfer function, relation (4), and Bode plots are shown in Figure 13. The input signal is a shock produced by an explosion at a distance of 2 km, which is recorded by the Chaparral sensor ('cha', the reference) and the EMFIT sensors ('pla').

$$y(s) = \frac{6.90969s - 294.546}{0.00334077s2 + 4.35419s + 1} u(s) \quad (4)$$

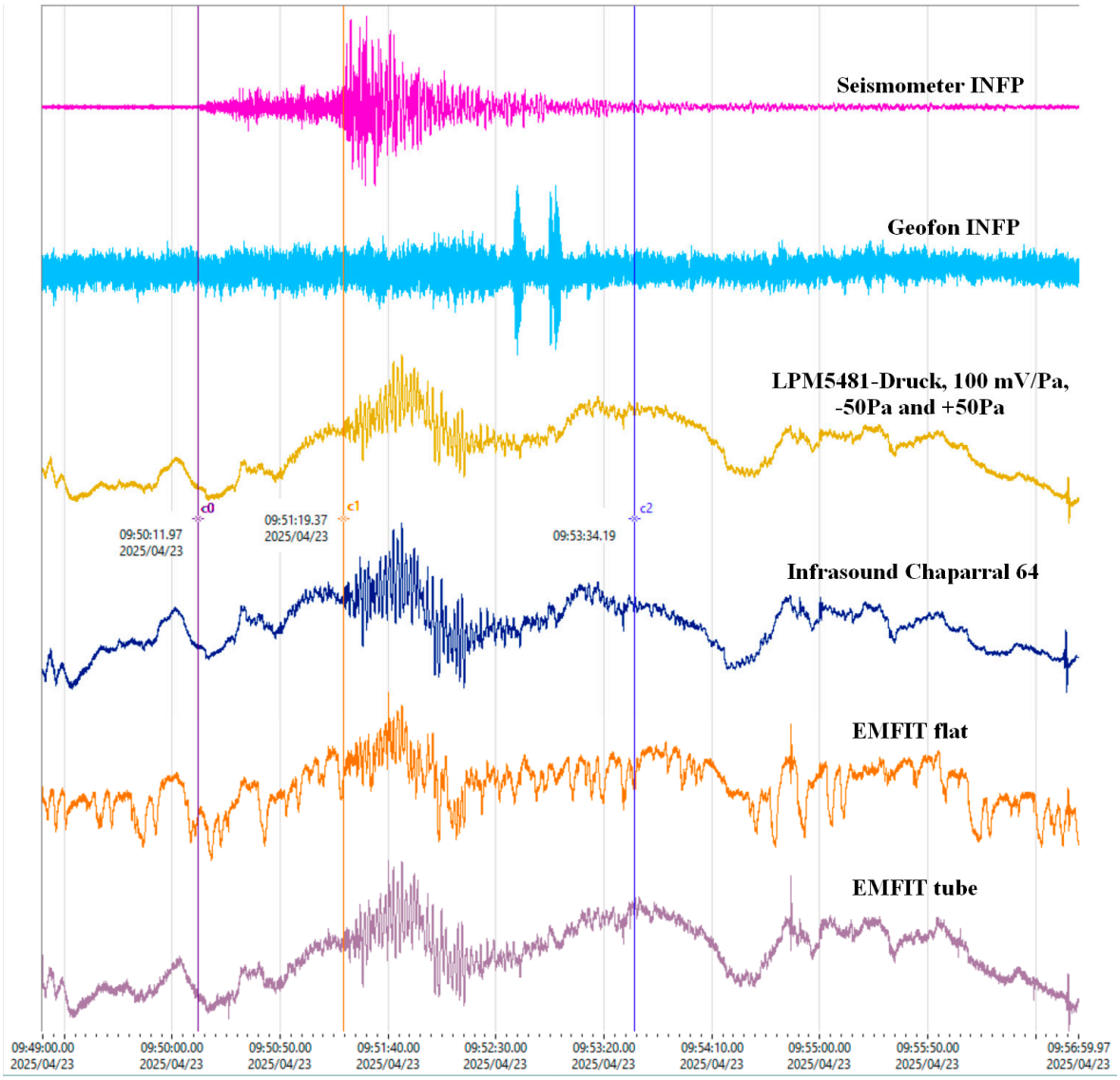


Figure 12. Recording of a 6.2 Mw earthquake located in the Sea of Marmara, 44 km SW of Esenyurt, Turkey, on 23 April 2025, at 09:49 UTC, with infrasound and Emfit sensors.

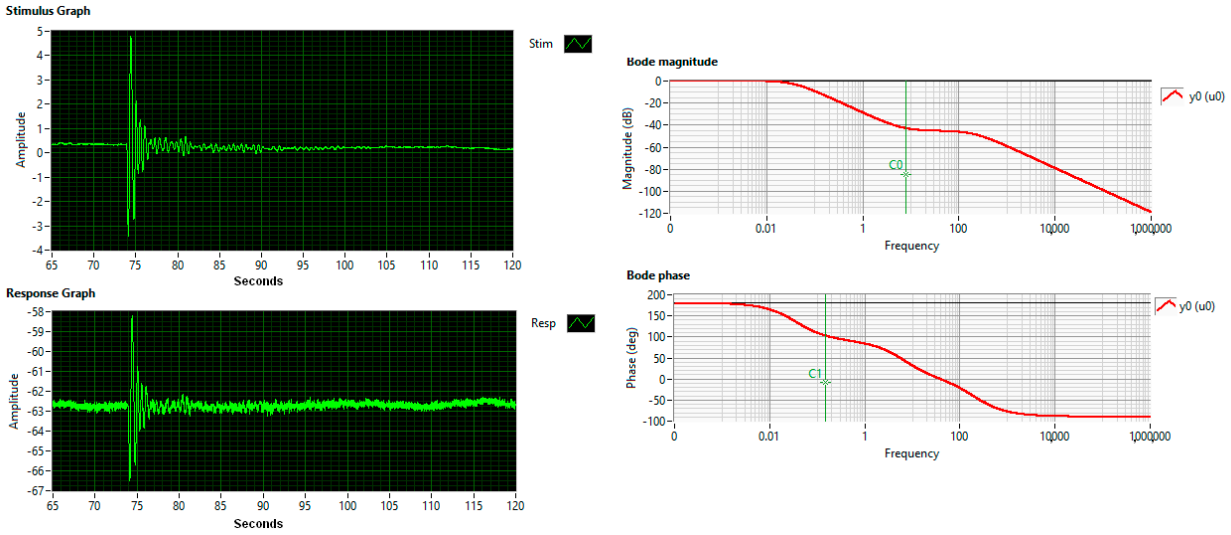


Figure 13. Bode Plots, Stimulus explosion ('cha'), Response EMFIT 'pla'.

4. Discussion

The preceding section presented the equipment, test conditions, and results, with emphasis on frequency response, the potential use of EMFIT sensors in the infrasound domain, and their ability to capture Rayleigh waves relevant to seismic tomography.

The first consideration concerns the test environment. Experiments were carried out in a basement, where temperature fluctuations were minimal (Figure 10). The test location, at 44.410700° latitude and 26.093800° longitude, is in an area without seismic activity, faults, or geological anomalies. The ambient noise is composed of road traffic and the trees in the park where the building is located. The chamber was not acoustically isolated, allowing reflections from the semi-cylindrical ceiling and flat ends, which likely contributed to the resonant features in Figures 8 and 9. These are not intrinsic to the Chaparral reference sensor but reflect the test setup. Ambient noise from outside the chamber was also present, but its effect was reduced by applying a ± 2 Hz band-pass filter (Figure 7).

A second peculiarity relates to the audio test signal. As shown in Figure 6 (spectrogram) and Figure 7 (time series), the software signal generator did not produce a continuous wave but generated bursts at programmed frequencies. While different from laboratory-grade signal generators, the results remain valid because the Chaparral reference sensor was measured under identical conditions. Thus, the tests represent realistic working conditions rather than strictly controlled laboratory experiments, such as those described in [62].

Differences in sensor placement (Figure 4b) also contributed to variations. For example, the Chaparral sensor was mounted inside a tube, whereas EMFIT sensors had different positions relative to the source. This is reflected in Figures 8 and 9, where deviations (e.g., at 39.5 Hz) appear consistently across both the Chaparral (cha) and EMFIT sensors (tbI).

Figure 10 highlights the sensitivity of EMFIT sensors to atmospheric pressure, consistent with their response to thickness variations under air pressure. In both Figures 10 and 11, a high-pass Butterworth filter at 2 Hz was applied to remove the DC component of the EMFIT signal. The observed correlation with Chaparral confirms EMFIT's capability in the infrasound domain. Under such conditions, the sampling rate could be reduced from 100 Hz to 10 Hz, enabling smaller file sizes, use of lower-cost digitizers, and reduced computational resources. For example, in Figure 2 a 16-bit acquisition module with a 1 Hz sampling rate was used. This would require the EMFIT preamplifier filter to be adjusted accordingly.

The ability to detect Rayleigh waves (Figure 11) is particularly significant, as it suggests that EMFIT sensors could be applied in seismic tomography. However, more data and additional sensors are needed to validate this.

The recording of the Marmara earthquake (Figure 12) was facilitated by specific conditions: one EMFIT sensor was mounted externally (Figure 3a), while another was coupled with an oscillating object, enhancing the signal.

Finally, the use of EMFIT sensors mounted inside or outside tubes represents a novel approach. The primary aim is to capture waves propagating through the ground. A buried tube with an externally mounted EMFIT sensor could enhance coupling with the soil. However, using closed tubes in outdoor environments may introduce issues such as condensation, unless proper thermal insulation is applied. EMFIT sensors could also be adapted for aquatic environments, provided the electronics are adequately protected. In this case, the water level itself could be monitored, with the caveat that wave direction must remain perpendicular to the sensor surface. Numerical simulations, such as those described in [53], further demonstrate how sensor dimensions and impact direction influence acoustic emission sensor performance—considerations equally relevant for EMFIT.

Comparative tests demonstrated that EMFIT sensors are capable of operating in the infrasound range and of recording Rayleigh waves generated by earthquakes, with responses comparable to those of the Chaparral reference sensor. Both tube-based and floor-mounted configurations produced similar response curves, with observed differences primarily attributable to chamber resonances and sensor positioning relative to the vibration source.

The analyses revealed a clear correlation between EMFIT signals and those of the reference sensor, including sensitivity to atmospheric pressure variations. The application of a 2 Hz high-pass filter successfully removed the continuous component, further confirming the suitability of EMFIT sensors for low-frequency monitoring. The recordings of Rayleigh waves from the Kamchatka earthquake and the Marmara Sea seismic event provide additional evidence of their applicability in seismological studies, with the added advantage of reduced sampling rates and lower data acquisition costs.

5. Conclusions

This study demonstrates that EMFIT sensors can be effectively employed for recording infrasound and Rayleigh-type seismic waves, yielding results comparable to established instruments such as the Chaparral and LPM 5481–Druck. The experimental setups—both on flat surfaces and in tubes—highlight the versatility of these sensors for diverse applications. One research direction we are currently pursuing is the use of EMFIT sensors in vertical tubes containing water. This approach is applied in geophysical measurements in both closed and open water wells, where geophone chains are inserted to measure velocity profiles as a function of depth.

The possibility of using EMFIT sensors for recording surface Rayleigh waves is interesting because it is applicable in noisy seismic tomography and in detecting subsurface activity. We chose long-range teleseismic to have mainly surface waves. Recordings with EMFIT sensors are much noisier than traditional ones. The specialized literature generally refers to piezoelectric film sensors (EMFIT is not a true piezoelectric sensor) and PVDF films, which also led to our tests. So, it is preferable to use broadband seismic sensors and use EMFITs if they are not available.

The tests were conducted using an infrasound sensor as a reference. To enable comparison and determine a transfer function, the same response area was selected, but differences remain, as shown in Figures 11 and 12. In the NIEP network of infrasound sensors, the signal is captured from the air. The EMFIT sensor functions as an "ear" for detecting ground noise and is isolated from air vibrations by sound-absorbing materials. Old data from the NIEP database indicate that EMFIT sensors can be used, but the relevant research has been lost, if it ever existed. Comparing the old records with the new ones suggests that the sensors may not be of the same type, even if they share the same name.

The findings support the use of EMFIT sensors as a complementary and cost-effective alternative for geophysical monitoring. Nonetheless, further research and extended field testing are required to fully validate their large-scale applicability.

Author Contributions: Conceptualization, V.-E.T.; methodology, V.-E.T. and I.-A.M.; software, V.-E.T.; validation, A.M. and C.I.; formal analysis, I.-A.M.; investigation, V.-E.T. and I.-A.M.; writing—original draft preparation, V.-E.T.; correspondent, V.-E.T.; supervision, C.I. All authors have read and agreed to the published version of the manuscript.

Funding: This research was funded by Nucleu Program project no PN23360101 and PN23360201, 101188365—TRANSFORM^2—HORIZON-INFRA-2024-DEV-01, and PNRR-III-C9-2022–I5 Establishment and operationalization of Competence Centers" competition, "Competence Center for Climate Change Digital Twin for Earth forecasts and societal redressment: DTEClimate" project, contract no.760008/30.12.2022, code 7/16.11.2022.

Institutional Review Board Statement: Not applicable.

Informed Consent Statement: Not applicable.

Data Availability Statement: The raw data supporting the conclusions of this article will be made available by the authors on request.

Acknowledgments: Financial support of projects 101188365—TRANSFORM^2—HORIZON-INFRA-2024-DEV-01 and PNRR- DTEClimate 760008/30.12.2022 for this study is gratefully acknowledged.

Conflicts of Interest: The authors declare no conflicts of interest.

References

1. Kärki, S.; Lekkala, J. A lumped-parameter transducer model for piezoelectric and ferroelectret polymers. *Measurement* **2012**, *45*, 453–458. [CrossRef]
2. Grigorescu, L.; Diaconescu, I. The emfi material and their use. In *The Annals of "Dunarea de Jos" University of Galati*; Galati University Press: Galati, Romania, 2010; pp. 27–30.
3. Karki, S.; Kaariainen, M.; Lekkala, J. Measurement of heart sounds with EMFi transducer. In Proceedings of the 2007 29th Annual International Conference of the IEEE Engineering in Medicine and Biology Society, Lyon, France, 22–26 August 2007; pp. 1683–1686. [CrossRef]
4. Qiu, X.; Bian, Y.; Liu, J.; Xiang, Y.; Ding, T.; Zhu, W.; Xuan, F. Ferroelectrets: Recent developments. *IET Nanodielectrics* **2022**, *5*, 113–124. [CrossRef]
5. Lekkala, J.; Tuppurainen, J.; Paajanen, M. Material and Operational Properties of Large-Area Membrane Type Sensors for Smart Environments. In Proceedings of the XVII IMEKO World Congress, Dubrovnik, Croatia, 22–27 June 2003; pp. 2045–2048. Available online: http://www.imeko.org/publications/wc-2003/PWC-2003-TC18-005.pdf (accessed on 2 November 2025).
6. Kärki, S.; Salpavaara, T.; Lekkala, J. EMFi in wearable audio applications. In Proceedings of the 4th International Workshop on Wearable and Implantable Body Sensor Networks (BSN 2007), Aachen, Germany, 26–28 March 2007; Springer: Berlin/Heidelberg, Germany, 2007; Volume 13, pp. 86–91. [CrossRef]
7. Lekkala, J.; Paajanen, M.; Nykänen, H.; Antila, M.; Kataja, J. ElectroMechanical Film (EMFi)–Promising Electret Material for Active Control of Sound Applications. 2000. Available online: https://www.tib.eu/en/search/id/tema%3ATEMA20010904391/ElectroMechanical-film-EMFi-promising-electret/ (accessed on 2 November 2025).
8. Lekkala, J.; Salpavaara, T.; Kärki, S. EMFI-Versatile material for monitoring of human functions. In Proceedings of the 18th IMEKO World Congress 2006: Metrology for a Sustainable Development, Rio de Janeiro, Brazil, 17–22 September 2006; Volume 1, pp. 376–381.
9. Chiselev, A.-M.; Moraru, L. A Study of Far Field Directivity Pattern of Bio-Inspired EMFit Emitters. *IEEE Sens. J.* **2012**, *12*, 1372–1376. [CrossRef]
10. Jiménez, A.; Hernández, Á.; Ureña, J.; Pérez, M.C.; Álvarez, F.J.; De Marziani, C.; García, J.J.; Villadangos, J.M. EMFi-based ultrasonic transducer for robotics applications. *Sens. Actuators A Phys.* **2008**, *148*, 342–349. [CrossRef]
11. Sanomat, H.; Malysz, A.; Tv, T.G. *New EMFiT Take-off Force*; EMFiTECH Oy Ltd.: Vaajakoski, Finland, 2000.
12. Walter, M.; Eilebrecht, B.; Wartzek, T.; Leonhardt, S. The smart car seat: Personalized monitoring of vital signs in automotive applications. *Pers. Ubiquitous Comput.* **2011**, *15*, 707–715. [CrossRef]
13. Paajanen, M.; Lekkala, J.; Kirjavainen, K. ElectroMechanical Film (EMFi)—A new multipurpose electret material. *Sens. Actuators A Phys.* **2000**, *84*, 95–102. [CrossRef]
14. Hamdi, O.; Mighri, F.; Rodrigue, D. Piezoelectric cellular polymer films: Fabrication, properties and applications. *AIMS Mater. Sci.* **2018**, *5*, 845–869. [CrossRef]
15. Antila, M.; Jari Kataja, B.P. Controlled directivity emfi panel loudspeaker. In *INTER-NOISE and NOISE-CON Congress and Conference Proceedings, Active 99*; International Institute of Noise Control Engineering (I-INCE): Reston, VA, USA, 1999; pp. 1171–1182.
16. Nykänen, H.; Antila, M.; Kataja, J.; Lekkala, J.; Uosukainen, S. Active control of sound based on utilizing EMFI-technology. In Proceedings of the International Symposium on Active Control of Sound and Vibration, ACTIVE 99, Fort Lauderdale, FL, USA, 2–4 December 1999; Institute of Noise Control Engineering: Reston, VA, USA, 1999; pp. 1159–1170.
17. Nykanen, H.; Antila, M.; Uosukainen, S.; Lekkala, J. Active increase of sound transmission loss of partitions based on utilizing EMFi panel actuators. *J. Acoust. Soc. Am.* **2000**, *108*, 2452. [CrossRef]
18. Pastell, M.; Kujala, M.; Aisla, A.-M.; Hautala, M.; Poikalainen, V.; Praks, J.; Veermäe, I.; Ahokas, J. Detecting cow's lameness using force sensors. *Comput. Electron. Agric.* **2008**, *64*, 34–38. [CrossRef]

19. Kressmann, R. New piezoelectric polymer for air-borne and water-borne sound transducers. *J. Acoust. Soc. Am.* **2001**, *109*, 1412–1416. [CrossRef]
20. Bauer, S.; Gerhard-Multhaupt, R.; Sessler, G.M. Ferroelectrets: Soft Electroactive Foams for Transducers. *Phys. Today* **2004**, *57*, 37–43. [CrossRef]
21. Rajala, S.; Lekkala, J. PVDF and EMFi sensor materials—A comparative study. *Procedia Eng.* **2010**, *5*, 862–865. [CrossRef]
22. Döring, J.; Bartusch, J.; Beck, U.; Erhard, A. EMFIT Ferroelectret Film Transducers for Non-Contact Ultrasonic Testing. 2006, pp. 1–10. Available online: https://www.researchgate.net/profile/Uwe_Beck/publication/237643046_EMFIT_Ferroelectret_Film_Transducers_for_Non-Contact_Ultrasonic_Testing/links/0c960526b4c5ac83df000000/EMFIT-Ferroelectret-Film-Transducers-for-Non-Contact-Ultrasonic-Testing.pdf?origin=publication_list (accessed on 2 November 2025).
23. Martin, A.J.; Alonso, A.H.; Ruiz, D.; Gude, I.; De Marziani, C.; Perez, M.C.; Alvarez, F.J.; Gutierrez, C.; Urena, J. EMFi-Based Ultrasonic Sensory Array for 3D Localization of Reflectors Using Positioning Algorithms. *IEEE Sens. J.* **2015**, *15*, 2951–2962. [CrossRef]
24. Sotgiu, E.; González-Losada, P.; Pinto, R.M.R.; Yang, H.; Faraji, M.; Vinayakumar, K.B. Pyroelectrically Charged Flexible Ferroelectret-Based Tactile Sensor for Surface Texture Detection. *Electronics* **2022**, *11*, 2329. [CrossRef]
25. Tikander, M.; Penttinen, H. Sound quality differences between electret film (EMFIT) and piezoelectric under-saddle guitar pickups. In Proceedings of the Audio Engineering Society-120th Convention Spring Prepr 2006, Paris, France, 20–23 May 2006; pp. 1221–1231.
26. Čechák, J. Seismic Sensor Using Piezo-Film. *AiMT Adv. Mil. Technol.* **2008**, *3*, 1–12.
27. Li, M.; Zang, H.; Long, J.; Sun, S.; Zhang, Y. Flexible Pressure Sensors Based on Polyvinylidene Fluoride: A Critical Review. *Materials* **2025**, *18*, 615. [CrossRef]
28. Li, X.; Wong, V.-K.; Yousry, Y.M.; Lim, D.B.K.; Subhodayam, P.T.C.; Yao, K.; Feng, L.; Qian, X.; Fan, Z. Surface Crack Monitoring by Rayleigh Waves with a Piezoelectric-Polymer-Film Ultrasonic Transducer Array. *Sensors* **2023**, *23*, 2665. [CrossRef]
29. Du, Q.; Pan, Y.; Xin, Y. Research and application of Rayleigh wave extraction method based on microtremors signal analysis. *Front. Phys.* **2023**, *11*, 1158049. [CrossRef]
30. Mihai, A.; Petrescu, L.; Moldovan, I.A.; Radulian, M. Investigating Rayleigh Wave Dispersion Across the Carpathian Orogen in Romania. *Geosciences* **2025**, *15*, 228. [CrossRef]
31. Liu, J.; Tang, Y.; Tao, K.; Yu, C.; Chen, J.; Ning, J.; Chen, Y.J.; Feng, Y. A new stacking technique in ambient noise tomography. *Earthq. Sci.* **2010**, *23*, 627–636. [CrossRef]
32. Safarkhani, M.; Shirzad, T. Improving C1 and C3 empirical Green's functions from ambient seismic noise in NW Iran using RMS ratio stacking method. *J. Seismol.* **2019**, *23*, 787–799. [CrossRef]
33. Foti, S.; Parolai, S.; Albarello, D.; Picozzi, M. Application of Surface-Wave Methods for Seismic Site Characterization. *Surv. Geophys.* **2011**, *32*, 777–825. [CrossRef]
34. Peng, H.; Li, J. Rayleigh wave attenuation tomography based on ambient noise interferometry: Methods and an application to Northeast China. *Geophys. J. Int.* **2024**, *237*, 1536–1553. [CrossRef]
35. Shirzad, T.; Assumpção, M.; Collaço, B.; Calhau, J.; Bianchi, M.B.; Barbosa, J.R.; Prieto, R.F.; Carlos, D.U. Shear wave velocities in the upper crust of the Quadrilátero Ferrífero, Minas Gerais: Rayleigh-wave tomography. *Braz. J. Geophys.* **2022**, *40*, 225–239. [CrossRef]
36. Vassallo, M.; De Matteis, R.; Bobbio, A.; Di Giulio, G.; Adinolfi, G.M.; Cantore, L.; Cogliano, R.; Fodarella, A.; Maresca, R.; Pucillo, S.; et al. Seismic noise cross-correlation in the urban area of Benevento city (Southern Italy). *Geophys. J. Int.* **2019**, *217*, 1524–1542. [CrossRef]
37. Cazzulani, G.; Alexakis, H. Comparison between acoustic emission sensors and piezoelectric patches for damage detection in concrete beams. In Proceedings of the 11th Eur Work Struct Heal Monit EWSHM 2024, Potsdam, Germany, 10–13 June 2024; pp. 1–8. [CrossRef]
38. Jiao, P.; Egbe, K.-J.I.; Xie, Y.; Nazar, A.M.; Alavi, A.H. Piezoelectric Sensing Techniques in Structural Health Monitoring: A State-of-the-Art Review. *Sensors* **2020**, *20*, 3730. [CrossRef]
39. Wang, G.; Qiu, W.; Liu, Y.; Bai, Y.; Cao, C.; Tang, F.; Wang, X.; Zhang, M. Damage detection for structural health monitoring using ultra-sensitive flexible piezoelectret sensors. *Struct. Heal. Monit.* **2023**, *22*, 2800–2812. [CrossRef]
40. Ferreira, P.M.; Machado, M.A.; Carvalho, M.S.; Vidal, C. Embedded Sensors for Structural Health Monitoring: Methodologies and Applications Review. *Sensors* **2022**, *22*, 8320. [CrossRef]
41. Li, Y.; Guo, S.; Su, Z.; Ding, K.; Loh, X.J. Lightweight and conformal acousto-ultrasonic sensing network for multi-scale structural health monitoring: A review. *FlexMat* **2025**, *2*, 4–29. [CrossRef]

42. Ealo, J.L.; Prieto, J.C.; Seco, F. Dynamic response estimation of multilayer ferroelectret-based transducers using lumped-element electromechanical models. In Proceedings of the 2009 IEEE International Ultrasonics Symposium, Rome, Italy, 20–23 September 2009; pp. 2754–2757. [CrossRef]
43. Räisänen, L.; Räisänen, H. Electro-responsive Polymer and its Sensor Applications. *MRS Proc.* **2005**, *889*, 0889-W02-01. [CrossRef]
44. Paajanen, M. The Cellular Polypropylene Electret Material-Electromechanical Properties. Ph.D. Thesis, Tampere University of Technology (TUT), Tampere, Finland, 2001; ISBN 951-38-5853-7.
45. Bain, A.K.; Chand, P. *Ferroelectrics*; Wiley-VCH Verlag GmbH & Co. KGaA: Weinheim, Germany, 2021.
46. Shi, J.; Wagih, M. Textile Tactile Senor Based on Ferroelectret for Gesture Recognition. *Eng. Proc.* **2022**, *15*, 8. [CrossRef]
47. Sahu, B.B.; Nayak, A.; Parti, S.K. Ferroelectric Sensor Materials: A short review. *Appl. Innov. Res.* **2023**, *4*, 167–175.
48. Batra, A.K.; Alomari, A. Fundamentals of Ferroelectric Materials. In *Power Harvesting via Smart Materials*; SPIE: Bellingham, WA USA, 2017; pp. 1–32. [CrossRef]
49. Thakur, V.N.; Zafer, A.; Yadav, S.; Kumar, A. Ferroelectric-dielectric composite pressure sensor. *Sens. Actuators A Phys.* **2019**, *297*, 111536. [CrossRef]
50. Damjanovic, D.; Muralt, P.; Setter, N. Ferroelectric sensors. *IEEE Sens. J.* **2001**, *1*, 191–206. [CrossRef]
51. Emfit Ltd. Calculating the Output Voltage of Emfit Sensors. Available online: http://www.emfit.com/ (accessed on 26 August 2011).
52. Emfit Ltd. *Emfit Sensors Linearity*; Rev C, 16.3.2003; Emfit Ltd.: Vaajakoski, Finland, 2003.
53. Tsangouri, E.; Aggelis, D.G. The influence of sensor size on Acoustic Emission waveforms-A numerical study. *Appl Sci.* **2018**, *8*, 168. [CrossRef]
54. Ono, K. Rayleigh Wave Calibration of Acoustic Emission Sensors and Ultrasonic Transducers. *Sensors* **2019**, *19*, 3129. [CrossRef]
55. Ono, K. Calibration methods of acoustic emission sensors. *Materials* **2016**, *9*, 508. [CrossRef]
56. Lan, H.; Yan, L.; Xiao, D.; Jiao, Z.; Chen, I.M. Surface-to-surface calibration of acoustic emission sensors. *Sens. Actuators A Phys.* **2012**, *174*, 16–23. [CrossRef]
57. Hatano, H.; Chaya, T.; Watanabe, S.; Jinbo, K. Reciprocity calibration of impulse responses of acoustic emission transducers. *IEEE Trans. Ultrason. Ferroelectr. Freq. Control.* **1998**, *45*, 1221–1228. [CrossRef]
58. *ISO/TR 13115:2011*; Non-Destructive Testing, Subcommittee SC 9 A Emission Testing. Non-Destructive Testing—Methods for Absolute Calibration of Acoustic Emission Transducers by the Reciprocity Technique. ISO: Geneva, Switzerland, 2011.
59. Monnier, T.; Seydou, D.; Godin, N.; Zhang, F.; Dia, S. Primary Calibration of Acoustic Emission Sensors by the Method of Reciprocity, Theoretical and Experimental Considerations. *J. Acoust. Emiss.* **2012**, *30*, 152–166.
60. Keprt, J. Method of Acoustic Emission Sensor Calibration. Available online: https://www.fekt.vut.cz/conf/EEICT/archiv/sborniky/EEICT_2005_sbornik/03-Doktorske_projekty/03-Kybernetika_a_automatizace/05-xkeprt01.pdf (accessed on 20 October 2025).
61. Keprt, J. Reciprocity and Step Function Calibration of Acoustic Emission Sensors. Available online: https://www.eeict.cz/eeict_download/archiv/sborniky/EEICT_2007_sbornik/03-doktorske_projekty/03-kybernetika_a_automatizace/06-xkeprt01.pdf (accessed on 2 November 2025).
62. Kober, J.; Prevorovsky, Z. In situ calibration of acoustic emission sensors. In Proceedings of the VIIIth International Workshop NDT in Progress (NDTP2015), Prague, Czech Republic, 12–14 October 2015; pp. 93–97.
63. Zaina, M.R.M.; Sama, S.A.; Hussain, A.; Azhari, C.H. Pitch and Timbre Determination of the Angklung. *Am. J. Appl. Sci.* **2009**, *6*, 24–29. [CrossRef]
64. Riggio, A.; Santulin, M. Earthquake forecasting: A review of radon as seismic precursor. *Boll. Geofis. Teor. Appl.* **2015**, *56*, 95–114. [CrossRef]
65. Nguyen, H.T.; Kreinovich, V.; Solopchenko, G.N.; Tao, C.W. Why Two Sigma? A Theoretical Justification. In *Soft Computing in Measurement and Information Acquisition*; Reznik, L., Kreinovich, V., Eds.; Springer: Berlin/Heidelberg, Germany, 2003; pp. 10–22. [CrossRef]
66. Mei, W.; Xu, Y.; Liu, L. Multiple model estimation under perspective of random-fuzzy dual interpretation of unknown uncertainty. *Signal Process.* **2024**, *217*, 109338. [CrossRef]
67. Kanshio, S. A review of hydrocarbon allocation methods in the upstream oil and gas industry. *J. Pet. Sci. Eng.* **2020**, *184*, 106590. [CrossRef]
68. Farrance, I.; Frenkel, R. Uncertainty of measurement: A review of the rules for calculating Uncertainty components through functional relationships. *Clin. Biochem. Rev.* **2012**, *33*, 49–75.
69. Morales-Simfors, N.; Wyss, R.A.; Bundschuh, J. Recent progress in radon-based monitoring as seismic and volcanic precursor: A critical review. *Crit. Rev. Environ. Sci. Technol.* **2020**, *50*, 979–1012. [CrossRef]
70. van Dalen, K.N.; Mikesell, T.D.; Ruigrok, E.N.; Wapenaar, K. Retrieving surface waves from ambient seismic noise using seismic interferometry by multidimensional deconvolution. *J. Geophys. Res. Solid. Earth.* **2015**, *120*, 944–961. [CrossRef]
71. Zoran, M.; Savastru, R.; Savastru, D.; Chitaru, C.; Baschir, L.; Tautan, M. Monitoring of radon anomalies in South-Eastern part of Romania for earthquake surveillance. *J. Radioanal. Nucl. Chem.* **2012**, *293*, 769–781. [CrossRef]

72. Galiana-Merino, J.J.; Molina, S.; Kharazian, A.; Toader, V.E.; Moldovan, I.A.; Gómez, I. Analysis of Radon Measurements in Relation to Daily Seismic Activity Rates in the Vrancea Region, Romania. *Sensors* **2022**, *22*, 4160. [CrossRef]
73. Keprt, J.; Benes, P. A Comparison of AE Sensor Calibration Methods. *J. Acoust. Emiss.* **2008**, *26*, 60.
74. *ASTM E1106-12(2021)*; Standard Test Method for Primary Calibration of Acoustic Emission Sensors. ASTM (American Society for Testing and Materials): West Conshohocken, PA, USA, 2012. [CrossRef]

Disclaimer/Publisher's Note: The statements, opinions and data contained in all publications are solely those of the individual author(s) and contributor(s) and not of MDPI and/or the editor(s). MDPI and/or the editor(s) disclaim responsibility for any injury to people or property resulting from any ideas, methods, instructions or products referred to in the content.